Numerical study of flow and thermal behaviour of lid-driven flows in cavities of small aspect ratios

Chin-Lung Chen[1,‡] and Chin-Hsiang Cheng[2,*,†,§]

[1]*Department of Mechanical Engineering, Lee-Ming Institute of Technology, Taipei, Taiwan, ROC*
[2]*Department of Mechanical Engineering, Tatung University, Taipei, Taiwan, ROC*

SUMMARY

Numerical study has been performed to investigate the effects of cavity shape on flow and heat transfer characteristics of the lid-driven cavity flows. Dependence of flow and thermal behaviour on the aspect ratio of the cavities is also evaluated. Three types of the cross-sectional shape, namely, circular, triangular, and rectangular, and four aspect ratios, $0.133, 0.207, 0.288$, and 0.5, are taken into account to construct twelve possible combinations; however, attention is focused on the small-aspect-ratio situations. Value of the Reynolds number considered in this study is varied between 100 and 1800. For the cases considered in this study a major clockwise vortex driven by the moving lid prevailing in the cavity is always observed. When the Reynolds number is fixed, the rectangular cavity produces strongest lid-driven flow, and the triangular cavity weakest. For the cases at small aspect ratio and low Reynolds number, the streamlines appear symmetric fore-and-aft with respect to the central line at $x/L = 0.5$. Data for the local and average Nusselt numbers are also provided. For rectangular cavities, it is observed that case 1/5R produces the highest average Nusselt number at any Reynolds number. Among the twelve possible geometric cases considered herein, the highest and lowest average Nusselt numbers are found with cases 1/6T and 1/2C, respectively. Copyright © 2006 John Wiley & Sons, Ltd.

KEY WORDS: forced convection; lid-driven; cavity flow

INTRODUCTION

Lid-driven cavity flows are of great interest in the past several decades, owing to their relevance to a number of engineering devices such as slider bearings [1, 2], wet clutches [3, 4], and gas lubrication systems [5, 6]. In the operation of a wet clutch, the contact between the grooved friction plate and the metal separator plate produces friction and then generates heat. The generated heat can only be removed by the fluid flow in the grooves. In addition, an air

---

*Correspondence to: Chin-Hsiang Cheng, Department of Mechanical Engineering, Tatung University, 40 Chung-shan N. Road, Sec. 3, Taipei 10451, Taiwan, ROC.
†E-mail: cheng@ttu.edu.tw
‡E-mail: chengjl@pchome.com.tw
§Professor.

Copyright © 2006 John Wiley & Sons, Ltd.

gap lubrication unit is equipped with a series of horizontal cavities. A moving plate is placed at the top of the cavities in which the fluid is enclosed. The lubrication performance of the unit is then dependent on the cavity flow behaviour and the pressure distribution in the cavity.

A number of reports, for example, Theodossiou and Sousa [7] and Ghia *et al.* [8], were published to present numerical algorithms for solving the fluid flow equations. In these reports, the lid-driven cavity flows are frequently regarded as a benchmark problem for testing the relative performance of the numerical schemes. In addition, Freitas *et al.* [9] performed experimental and numerical investigation of three-dimensional forced convection heat transfer in a rectangular cavity filled with liquid water. In this report, results for a cavity flow at a Reynolds number of 3200 have been presented and the Taylor–Gortler-like vortices were observed. Recently, Migeon *et al.* [10] performed experimental investigation of laminar forced convection inside the two-dimensional square, rectangular, and semi-circular water cavities at a Reynolds number of 1000. Lately, the same group of authors extended their experimental study to the three-dimensional square and rectangular water cavity flows [11].

It appears that most previous studies regarding the flow and thermal behaviour of the lid-driven cavity flows were focused mainly on the flows in the rectangular cavities [7–11]. There were few reports that dealt with cavities with complex shapes. More recently, Chen and Cheng [12, 13] investigated flow and thermal characteristics in an arc-shape cavity, and found very different flow features between the flows in the rectangular and the arc-shape cavities. According to the data obtained, it was observed that the cavity shape may have profound influence on the flow pattern and heat transfer characteristics of the cavity flows. Unfortunately, the effects of cavity geometry on the flow and thermal behaviour have not been sufficiently studied. In these circumstances, the major aim of the present study is to numerically study the geometry effects of the cavity on the flow and convective heat transfer characteristics of the lid-driven cavity flows. Dependence of the flow pattern and thermal characteristics on the shape and the aspect ratio of the cavities is of major concern.

Physical models of the lid-driven cavities are shown in Figure 1. In this study, three types of the cross-sectional shape of the cavity, namely, circular, triangular, and rectangular, are considered. For each type of shape, four aspect ratios (H/L), 0.133, 0.207, 0.288 and 0.5, are taken into account so as to construct twelve possible geometric combinations. The complex-shape bottom wall is stationary and is maintained at a uniform higher temperature T_H. The lid of the cavity is maintained at a lower temperature T_L and moves at a steady velocity u_0. The cavities are of height H and width L. The twelve test cases are listed in Table I. Each case is named based on the shape of the cavity and the aspect ratio. For example, case 1/4T is with the triangular cavity of $H/L = 0.288$ and case 1/2R is with the rectangular cavity of $H/L = 0.5$. However, in this study attention is focused on the small-aspect-ratio situations, cases 1/6C, 1/6T, and 1/6R. Value of the Reynolds number (Re) considered in this study is varied between 100 and 1800, and the Prandtl number (Pr) is assigned to be 0.71 for air flow.

THEORETICAL ANALYSIS

Governing equations and boundary conditions

The fluid flow is assumed to be two-dimensional, steady, incompressible, and laminar. Fluid properties are assumed to be constant, and the body forces are neglected. The continuity,
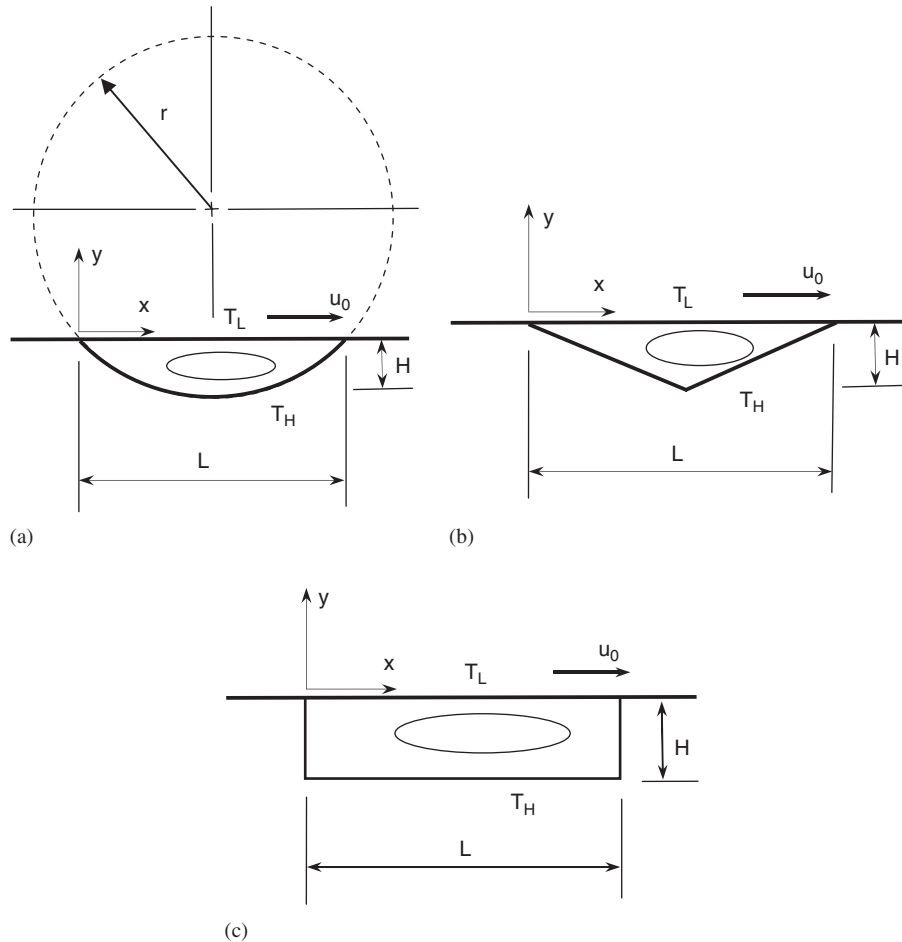

Figure 1. Physical configuration: (a) circular cavity; (b) triangular cavity; and (c) rectangular cavity.

momentum, and energy equations governing the velocity and temperature fields in the cavity are expressed on Cartesian coordinates as

$$u_x + v_y = 0 \tag{1}$$

$$uu_x + vu_y = -\frac{1}{\rho}p_x + v(u_{xx} + u_{yy}) \tag{2}$$

$$uv_x + vv_y = -\frac{1}{\rho}p_y + v(v_{xx} + v_{yy}) \tag{3}$$

$$uT_x + vT_y = \alpha(T_{xx} + T_{yy}) \tag{4}$$

The stream function-vorticity formulation is adopted in this study to express these above equations. Meanwhile, the curvilinear coordinates (ξ, η) are required when one deals with

Table I. Test cases.

Cases	Circular	Triangular	Rectangular
$H/L = 0.133$	1/6C	1/6T	1/6R
$H/L = 0.207$	1/5C	1/5T	1/5R
$H/L = 0.288$	1/4C	1/4T	1/4R
$H/L = 0.5$	1/2C	1/2T	1/2R

the irregular solution domain. Based on the curvilinear coordinates, vorticity (ω) and stream function (ψ) are expressed as

$$\omega = v_x - u_y = (\xi_x v_\xi + \eta_x v_\eta) - (\xi_y u_\xi + \eta_y u_\eta) \tag{5a}$$

and

$$u = \psi_y = \xi_y \psi_\xi + \eta_y \psi_\eta \tag{5b}$$

$$v = -\psi_x = -(\xi_x \psi_\xi + \eta_x \psi_\eta) \tag{5c}$$

respectively. The following dimensionless parameters are defined in prior to derive the dimensionless forms of the governing equations as

$$X = x/L, \quad Y = y/L, \quad U = u/u_0, \quad V = v/u_0, \quad \Psi = \psi/u_0 L$$

$$\Omega = \omega L/u_0, \quad Re = u_0 L/v, \quad Pr = v/\alpha \tag{6}$$

Introducing the stream function-vorticity formulation, curvilinear coordinates, and the dimensionless parameters into the governing equations yields

$$a\Psi_{\eta\eta} - 2b\Psi_{\xi\eta} + c\Psi_{\xi\xi} = -J\Omega \tag{7}$$

$$\Psi_\eta \Omega_\xi - \Psi_\xi \Omega_\eta = (a\Omega_{\eta\eta} - 2b\Omega_{\xi\eta} + c\Omega_{\xi\xi})/JRe \tag{8}$$

$$\Psi_\eta \theta_\xi - \Psi_\xi \theta_\eta = (a\theta_{\eta\eta} - 2b\theta_{\xi\eta} + c\theta_{\xi\xi})/(JPrRe) \tag{9}$$

where

$$a = X_\eta^2 + Y_\eta^2 \tag{10a}$$

$$b = X_\xi X_\eta + Y_\eta Y_\xi \tag{10b}$$

$$c = X_\xi^2 + Y_\xi^2 \tag{10c}$$

$$J = X_\eta Y_\xi - X_\xi Y_\eta \tag{10d}$$

The non-slip boundary conditions for velocity components and the isothermal condition on the moving lid are given in dimensionless form as

$$\text{On the moving lid:} \quad U = 1, \quad V = 0, \quad \Psi = 0, \quad \Omega = -(X_\xi U_\eta)/J \tag{11}$$

On the other hand, the boundary conditions on the complex-shape bottom wall are prescribed by

$$\text{On the bottom wall:} \quad U = 0, \quad V = 0, \quad \Psi = 0, \quad \Omega = -(Y_\xi V_\eta - X_\xi U_\eta)/J \tag{12}$$

NUMERICAL METHODS

Equations (7)–(9) are then discretized into a set of simultaneous algebraic equations on the curvilinear coordinates (ξ, η). The obtained discretization expressions for Ψ, Ω, and θ are solved individually. Equation (7), the Poisson equation of stream function, is solved by the successive over-relaxation (SOR) method, and Equations (8) and (9), the vorticity transport equation and the energy equation, are solved by the finite-volume method. Further information regarding theses numerical methods is available in References [12–14].

The curvilinear coordinates, $\xi = \xi(X, Y)$ and $\eta = \eta(X, Y)$, are obtained by solving the following two elliptic Poisson equations:

$$\frac{\partial^2 \xi}{\partial X^2} + \frac{\partial^2 \xi}{\partial Y^2} = P(X, Y) \tag{13}$$

$$\frac{\partial^2 \eta}{\partial X^2} + \frac{\partial^2 \eta}{\partial Y^2} = Q(X, Y) \tag{14}$$

where P and Q are two arbitrary functions specified to adjust the local density of the grids. Meanwhile, the orthogonality of the generated grids can be improved by carefully setting the boundary conditions associated with Equations (13) and (14). A grid system of 101×101 grids for the computation domain is adopted typically in the analysis after a careful check for the grid independence of the numerical solution is made, in order to ensure the accuracy and validity of the numerical schemes.

RESULTS AND DISCUSSION

Flow and thermal fields

Numerical results of flow fields and temperature distributions for various cases are displayed in the section with streamlines and isotherms, respectively. In each plot, data of maximum and minimum values of the variables of interest are shown for a quantitative comparison.

Effects of Reynolds number and aspect ratio on the flow pattern and temperature distribution for circular cavity flows are shown in Figure 2. For the small-aspect-ratio cases ($H/L = 0.133$), a shear-driven clockwise vortex is observed. At $H/L = 0.133$ and $Re = 100$, the centre of the vortex is located nearly at the centre of the cavity, and the streamlines and isotherms appear symmetric fore-and-aft with respect to the central line at $x/L = 0.5$. This symmetry feature is part of the nature of the Stokes flows at low Reynolds number, which have been visualized by a number of authors, for example, Taneda [15]. However, an increase in the Reynolds number causes the centre of the vortex to move toward the right corner of the cavity, and the symmetry feature is no longer visible. When the aspect ratio is elevated, the strength of the vortex is appreciably increased, and a second counter-clockwise vortex may appear in the lower left area of the cavity. Meanwhile, based on the isotherms plotted in Figure 2, it is clearly seen that the vortex motion produces a convection effect in the area near the right corner, where the thermal stratification is obviously blurred. Extent and strength of the convection region near the right corner increase with either Reynolds number or the aspect ratio. Also, since a higher temperature gradient indicates a higher heat transfer rate, based on the distribution of the isotherms adjacent to the walls, the higher heat transfer rates may be located in the top-left and the bottom-right surface areas for the circular cavities.

Similar effects of Reynolds number and aspect ratio on the flow patterns and temperature distributions in the triangular cavities are illustrated in Figure 3. Again, the streamlines look symmetric with respect to the central line at $x/L = 0.5$ for the case at $H/L = 0.133$ and $Re = 100$. However, the strength of the vortex is relatively weaker in the triangular cavities than in the circular cavities at the same Reynolds numbers and aspect ratios. For the triangular cavities, the higher heat transfer rates may also be observed in the top-left and the bottom-right surface areas.

Figure 4 shows the effects of Reynolds number and aspect ratio on the flow patterns and temperature distributions in the rectangular cavities. For the case at lower aspect ratio and low Reynolds number, it is expected to observe two nearly symmetric vortices in the rectangular cavity since in this situation the flow approaches the Stokes-flow condition [15]. The plot of $H/L = 0.133$ and $Re = 100$ agrees with this expectation, and for this case two nearly symmetric clockwise vortices are observed in the cavity. When the value of Reynolds number is increased, the right vortex becomes stronger while the left one becomes weaker. At $Re = 500$, the left vortex completely disappears. For the rectangular cavities, it is found that higher heat transfer rates are located in the areas near the left corner on the moving lid surface and near the upper corner on the right wall. The higher heat transfer rate near the left corner on the colder lid surface is caused by the impingement of the hot plume rising along the vertical left wall. On the other hand, the down washing of the cold stream from the lid surface forms a thermal boundary layer on the right wall so as to result in a higher heat transfer rate near the upper corner on the right wall. Note that among the three types of cross-sectional shapes considered, the rectangular cavity produces strongest lid-driven flow and the triangular cavity weakest at the same Reynolds number.

$\Psi_{min} = -0.0197147$ $\Psi_{max} = 0$ $\theta_{min} = 0$ $\theta_{max} = 1$

Re = 100, H/L=0.133

$\Psi_{min} = -0.0195382$ $\Psi_{max} = 0$ $\theta_{min} = 0$ $\theta_{max} = 1$

Re = 1000, H/L=0.133

$\Psi_{min} = -0.0194547$ $\Psi_{max} = 0$ $\theta_{min} = 0$ $\theta_{max} = 1$

Re = 1500, H/L=0.133

$\Psi_{min} = -0.0428751$ $\Psi_{max} = 0.00249193$ $\theta_{min} = 0$ $\theta_{max} = 1$

Re = 1500, H/L=0.288

$\Psi_{min} = -0.0780323$ $\Psi_{max} = 0.00238655$ $\theta_{min} = 0$ $\theta_{max} = 1$

Re = 1500, H/L=0.5

Streamlines   **Isotherms**

Figure 2. Effects of Reynolds number and aspect ratio on flow pattern and temperature
distribution for circular cavity flows.

Ψ_{min} = -0.0183122 Ψ_{max} = 0 θ_{min} = 0 θ_{max} =1

Re = 100, H/L= 0.133

Ψ_{min} = -0.0176932 Ψ_{max} = 0 θ_{min} = 0 θ_{max} =1

Re = 1000, H/L= 0.133

Ψ_{min} = -0.0172493 Ψ_{max} = 0 θ_{min} = 0 θ_{max} =1

Re = 1800, H/L= 0.133

Ψ_{min} = -0.0308144 Ψ_{max} = 0.00218753 θ_{min} = 0 θ_{max} =1

Re = 1800, H/L= 0.288

Ψ_{min} = -0.0446144 Ψ_{max} = 0.00536299 θ_{min} = 0 θ_{max} =1

Re = 1800, H/L= 0.5
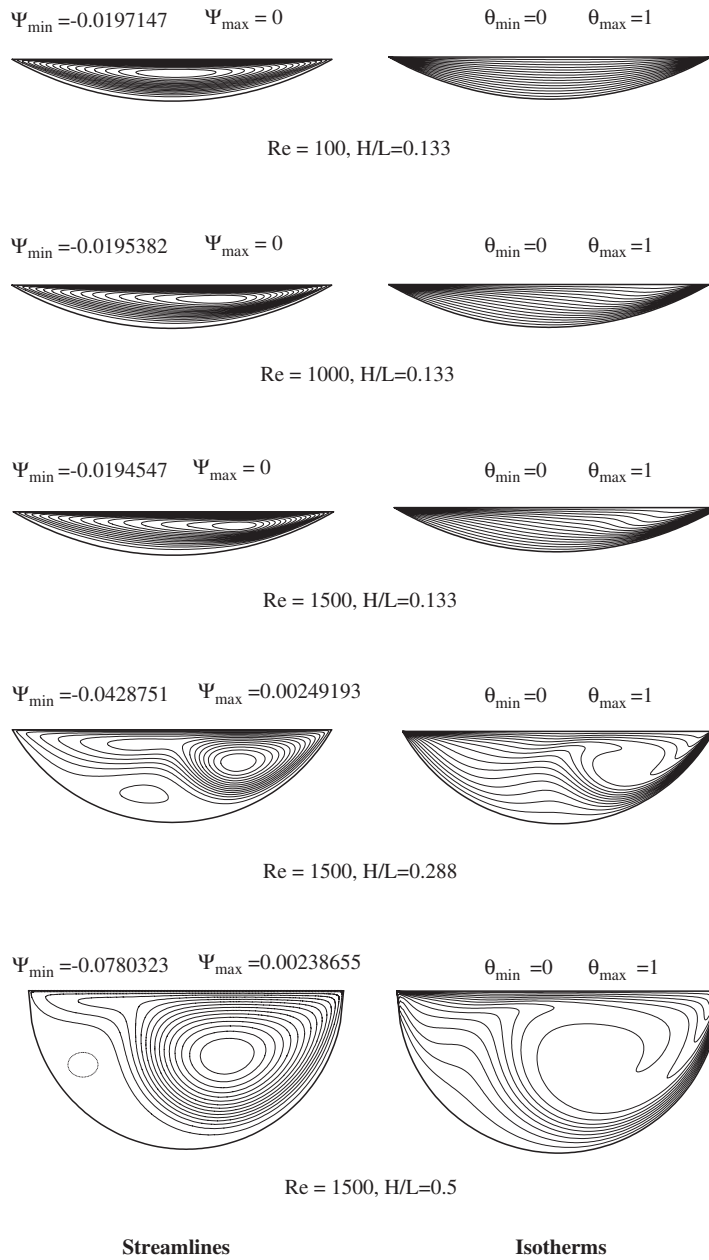
Streamlines   **Isotherms**

Figure 3. Effects of Reynolds number and aspect ratio on flow pattern and temperature
distribution for triangular cavity flows.

$\Psi_{min} = -0.0232358 \quad \Psi_{max} = 0$ $\theta_{min} = 0 \quad \theta_{max} = 1$

Re = 100, H/L = 0.133

$\Psi_{min} = -0.0244295 \quad \Psi_{max} = 0$ $\theta_{min} = 0 \quad \theta_{max} = 1$

Re = 300, H/L = 0.133

$\Psi_{min} = -0.0252544 \quad \Psi_{max} = 0$ $\theta_{min} = 0 \quad \theta_{max} = 1$

Re = 500, H/L = 0.133

$\Psi_{min} = -0.0655426 \quad \Psi_{max} = 0$ $\theta_{min} = 0 \quad \theta_{max} = 1$

Re = 500, H/L = 0.288

$\Psi_{min} = -0.115985 \quad \Psi_{max} = 0.0047525$ $\theta_{min} = 0 \quad \theta_{max} = 1$
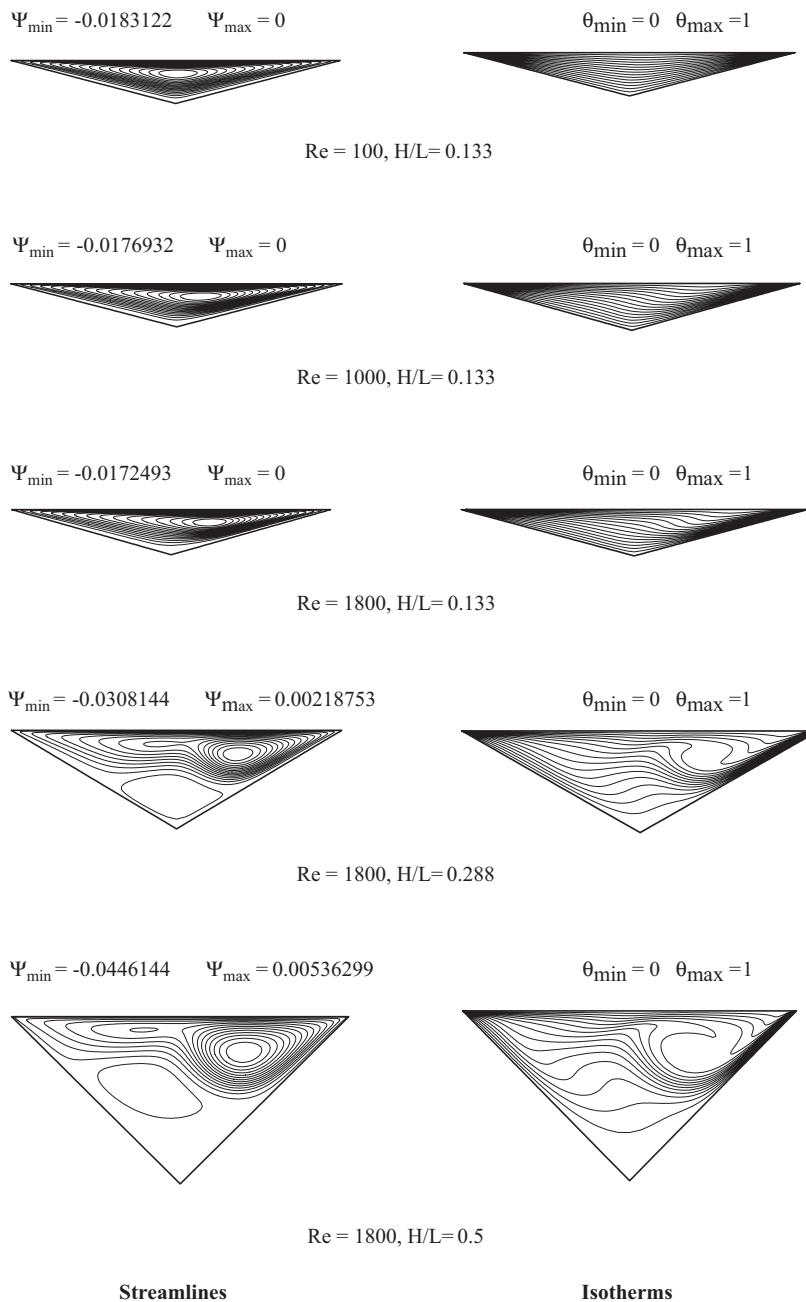
Re = 500, H/L = 0.5
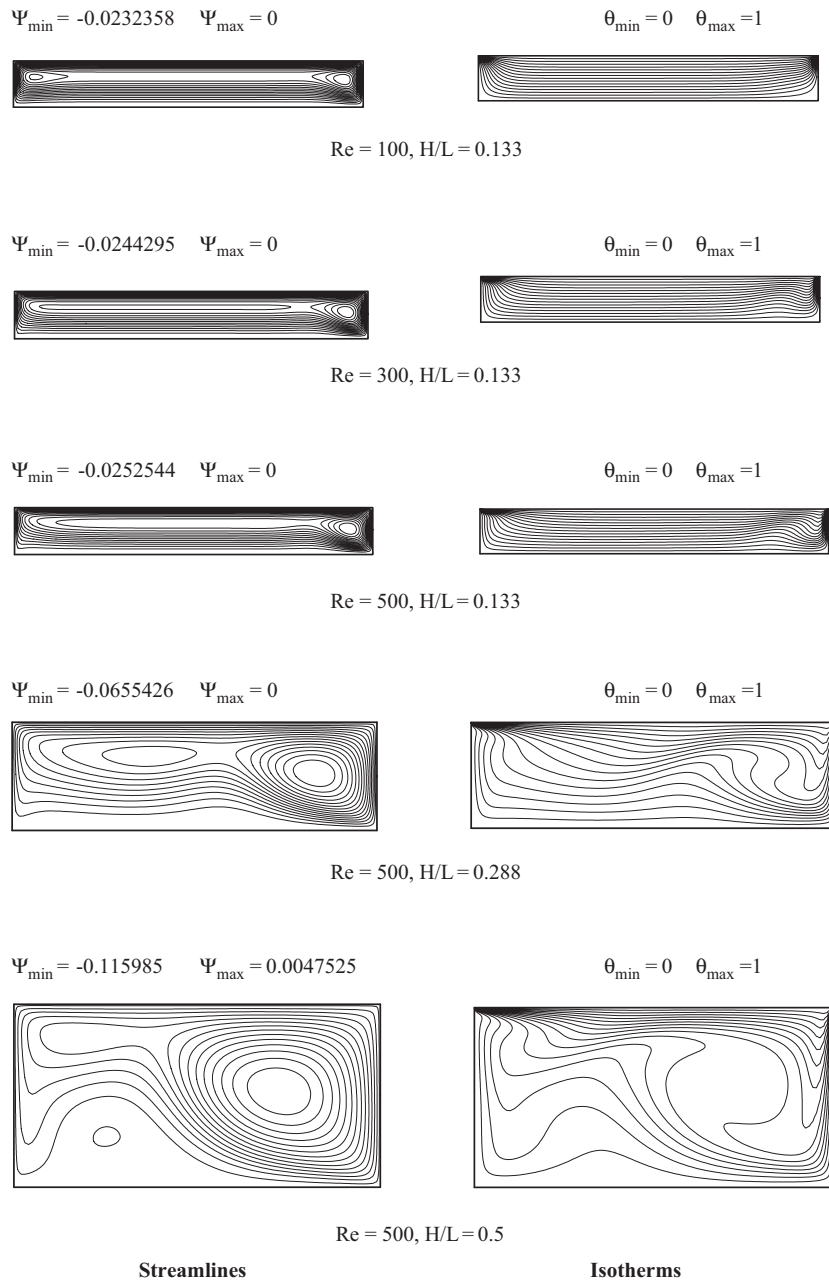
Streamlines **Isotherms**

Figure 4. Effects of Reynolds number and aspect ratio on flow pattern and temperature distribution for rectangular cavity flows.

Heat transfer performance

The obtained numerical solutions for temperature distributions are used to further evaluate heat transfer performance of the cavity flows. Meanwhile, the solutions of the velocity field are used to determine the shear stress on the moving lid. Local Nusselt number on the moving lid surface representing the local heat transfer performance is defined by

$$Nu_x = \frac{h_x L}{k} = \left. \frac{L}{T_H - T_L} \frac{\partial T}{\partial y} \right|_{\text{moving lid}} \tag{15}$$

where h_x is the local heat transfer coefficient.

Based on the results of the local Nusselt number, average Nusselt number on the moving lid surface can be further evaluated by integration as

$$Nu = \frac{\bar{h} L}{k} = \int_0^1 Nu_x \, dX \tag{16}$$

where the average heat transfer coefficient $\bar{h}$ is given by

$$\bar{h} = \frac{1}{L} \int_0^L h_x \, dX \tag{17}$$

Note that the magnitude of the average Nusselt number represents the overall heat transfer performance of the cavity flow.

On the other hand, local friction factor on the moving lid is defined in terms of the local shear stress as

$$f_x = \frac{\tau_x}{\rho u_0^2} = \left. \frac{\mu}{\rho u_0^2} \frac{\partial u}{\partial y} \right|_{\text{moving lid}} = \left. \frac{1}{Re} \frac{X_\xi}{J} U_\eta \right|_{\text{moving lid}} \tag{18}$$

Figure 5 shows the distributions of local Nusselt number on the moving lid for the circular, triangular, and rectangular cavities. In this figure, the value of Reynolds number is fixed at 500. The results presented in Figure 5(a) are for circular cavities with various aspect ratios. It is found that the magnitude of local Nusselt number is reduced if the aspect ratio is increased. This may be attributed to the increase in the heat transfer distance between the hot bottom wall and the cold lid accompanying the increase in the aspect ratio. Therefore, for case 1/6C, the magnitude of the local Nusselt number is always higher than other cases. The local Nusselt number reaches extremely high values at points near the two corners. Figure 5(b) shows the results of the local Nusselt number for the triangular cavity flows. Again, it is found that the case with smallest aspect ratio, case 1/6T, has the highest Nusselt number. However, the heat transfer characteristics of the rectangular cavity flows shown in Figure 5(c) exhibit a different feature. According to the data given in Figure 5(c), it is clearly seen that the highest heat transfer is with case 1/5R, not 1/6R. It seems that the heat transfer enhancement due to the increase in the vortex strength may compensate the heat transfer reduction due to the increase in the heat transfer distance, when the aspect ratio is elevated. Therefore, the Nusselt number is not monotonically increased with a decrease in the aspect ratio from 0.5 to 0.133, and apparently the heat transfer reaches a maximum at the aspect ratio of 0.207 with case 1/5R.
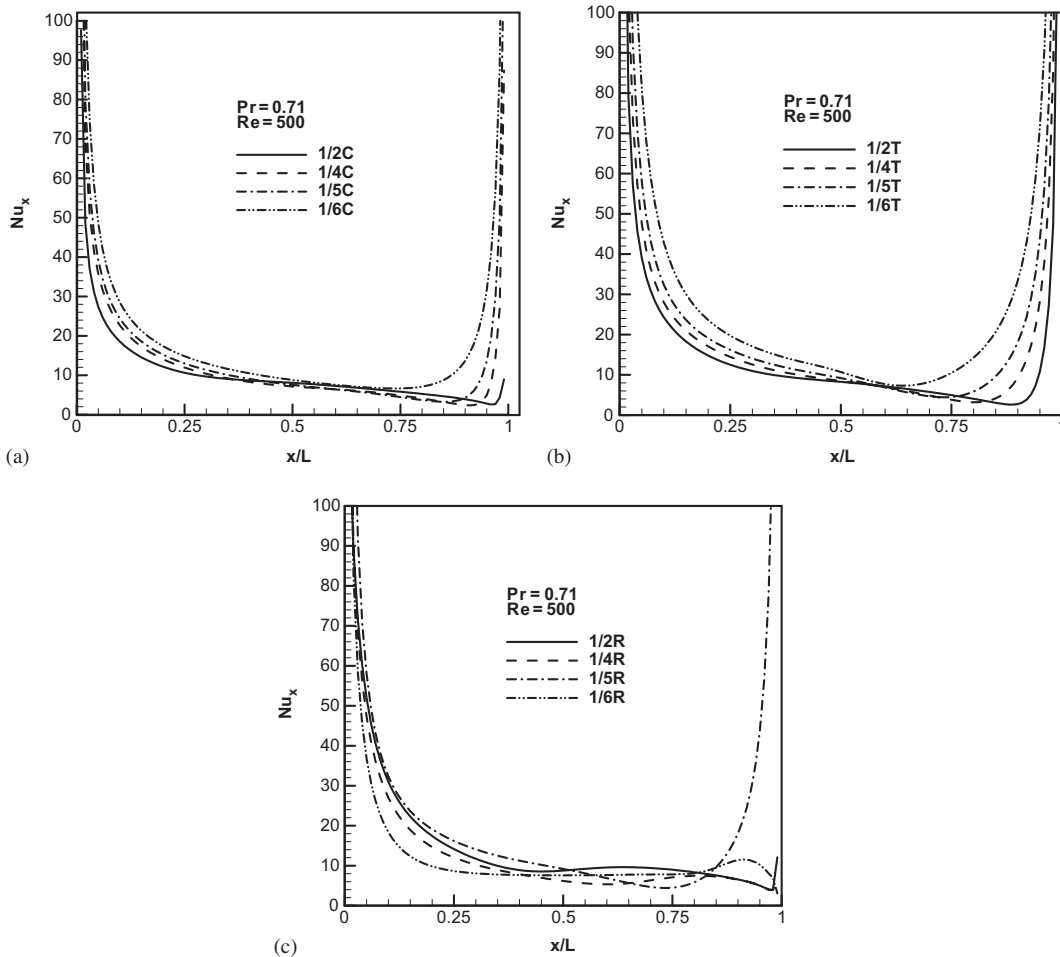
Figure 5. Distribution of local Nusselt number on the moving lid at $Re = 500$: (a) circular cavities; (b) triangular cavities; and (c) rectangular cavities.

In order to provide deeper insight into the effects of the Reynolds number and aspect ratio on overall heat transfer performance for various types of cavity flows, the data of average Nusselt number (Nu) as a function of the Reynolds number associated with the flows in circular, triangular, and rectangular cavities are provided in Figure 6(a), (b), and (c), respectively. It appears that the Reynolds number plays an important role in the heat transfer enhancement. In general, the average Nusselt number increases with the Reynolds number. The increase in Nu with Re becomes more obvious at a higher aspect ratio. For the cases with circular cavities shown in Figure 6(a), the curve of case 1/2C exhibits the poorest heat transfer performance. This reflects the fact observed in Figure 5(a) that the magnitude of Nusselt number is reduced if the aspect ratio is increased. Similarly, in Figure 6(b) for the flows with triangular cavities, it is found that case 1/2T exhibits the poorest heat transfer performance and case 1/6T the best.
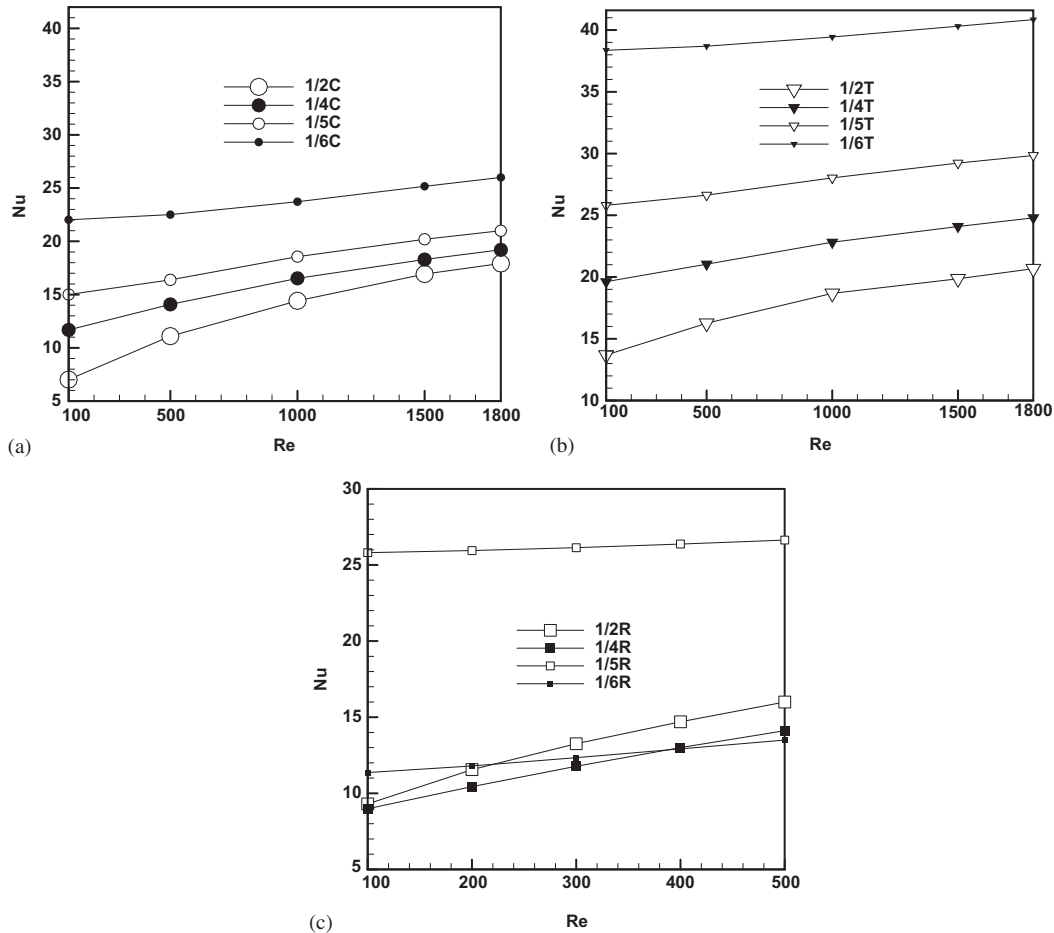
Figure 6. Average Nusselt number as a function of Reynolds number: (a) circular cavities;
(b) triangular cavities; and (c) rectangular cavities.

For the cases shown in Figures 6(a) and (b), the value of the Nusselt number monotonically increased with a decrease in the aspect ratio; however, the rectangular cavity flows shown in Figure 6(c) exhibit a different feature as already mentioned earlier. It is obvious that among these cases shown in Figure 6(c), case 1/5R produces the highest average Nusselt number at $Re \geqslant 200$. According to the data collected in this study, it is observed that among the twelve test cases considered herein, the highest and lowest average Nusselt numbers are found with cases 1/6T and 1/2C, respectively.

Effects of Reynolds number on the distributions of the local friction factor in terms of $f_x Re$ along the moving lid are shown in Figure 7. In this figure, the results for cases 1/6C, 1/6T, and 1/6R are provided in Figures 7(a), (b), and (c), respectively. In these cases, the aspect ratio is fixed at 0.133. For cases 1/6C and 1/6T, the value of $f_x Re$ increases with Reynolds number except for the area between $x/L = 0.6$ and 0.8, and the effects of Reynolds number are more significant in the left portion of the lid surface than in the right. In addition, the curves
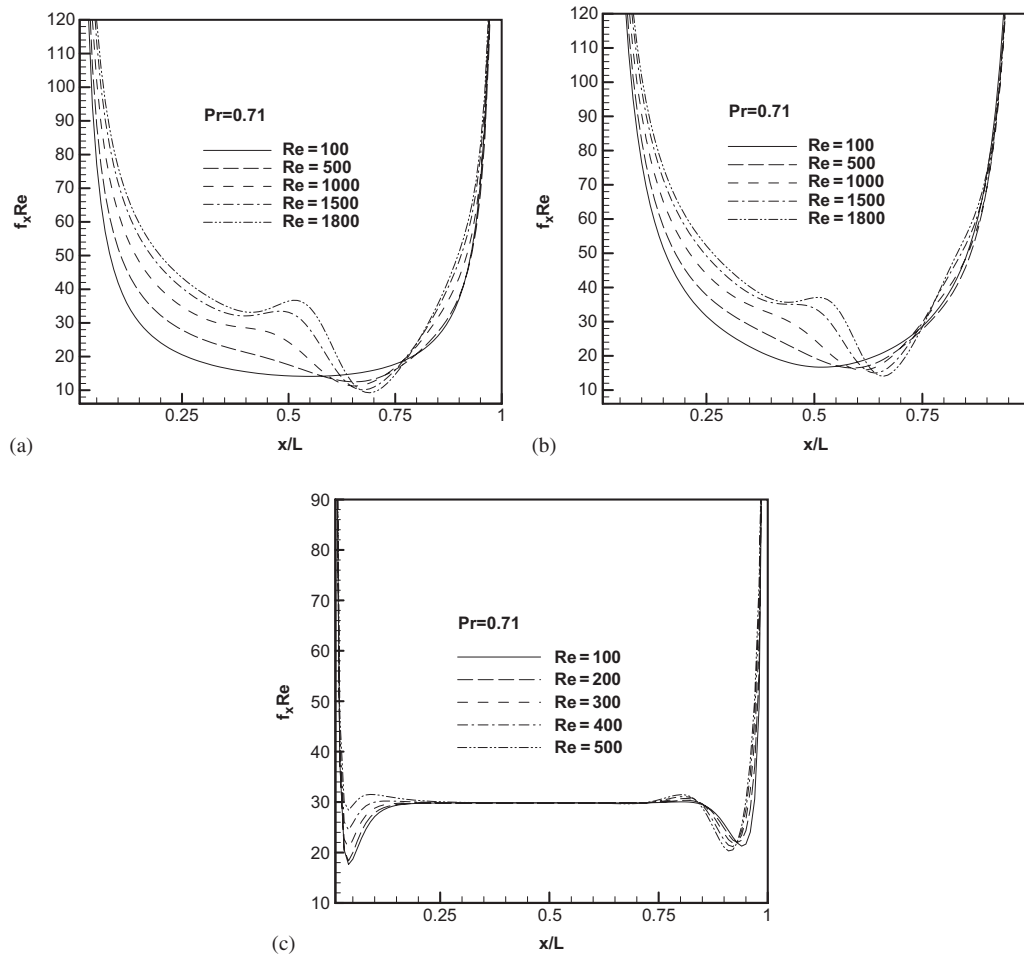
Figure 7. Effects of Reynolds number on the distributions of local friction factor on the moving lid at $H/L = 0.133$: (a) Case 1/6C; (b) Case 1/6T; and (c) Case 1/6R.

given in Figure 7(c) show that for case 1/6R the value of f_xRe increases with Reynolds number only for the areas near the two corners and the value reaches local minimum there. For the area between $x/L = 0.25$ and 0.75, an increase in Reynolds number from 100 to 500 produces no appreciable change in the friction factor. In all the three plots shown in Figure 7, the curves of $Re = 100$ relatively exhibit more symmetric feature as compared with those of higher Reynolds number.

CONCLUDING REMARKS

For the cases considered in this study a major clockwise vortex driven by the moving lid prevails in the cavity. When the Reynolds number is fixed, the rectangular cavity produces strongest lid-driven flow, and the triangular cavity weakest. For the cases at small aspect ratio

and low Reynolds number (say, 100), the streamlines appear symmetric fore-and-aft with respect to the central line at $x/L = 0.5$. This symmetry feature is the nature of the Stokes flows at low Reynolds number [15]. However, an increase in the Reynolds number causes the centre of the vortex to move toward the right corner of the cavity, and the symmetry feature is not visible. At a higher Reynolds number, the vortex motion produces a convection region near the right corner of the cavity, where the thermal stratification is obviously blurred. Based on the solutions obtained, for the circular and the triangular cavities, the higher heat transfer rates may be located in the top-left and the bottom-right surface areas. However, for the rectangular cavities, higher heat transfer rates are found in the areas near the left corner on the lid surface and near the upper corner on the right wall.

In general, the magnitude of the Nusselt number is reduced if the aspect ratio is increased. This may be attributed to the increase in the heat transfer distance between the hot bottom wall and the cold lid when the aspect ratio is increased. However, for the rectangular cavities, it is seen that the highest heat transfer is with case 1/5R, not 1/6R.

It is also found that the Reynolds number plays an important role in the heat transfer enhancement. In general, the average Nusselt number increases with the Reynolds number. The increase in *Nu* with *Re* becomes more obvious at a higher aspect ratio. It is observed that among the twelve test cases considered herein, the highest and lowest average Nusselt numbers are found with cases 1/6T and 1/2C, respectively.

NOMENCLATURE

a, b, c	coordinate transformation coefficients
f	friction factor
H	height of cavity
L	width of cavity
p	fluid pressure
Pr	Prandtl number
Re	Reynolds number
u, v	velocity components in x- and y-directions
u_0	velocity of moving lid
U, V	dimensionless velocity components in x- and y-directions
x, y	rectangular coordinates
X, Y	dimensionless rectangular coordinates

Greek symbols

α	thermal diffusivity of fluid
ξ, η	curvilinear coordinates
θ	dimensionless temperature
v	kinematic viscosity of fluid
ρ	density of fluid
ψ	stream function
Ψ	dimensionless stream function
ω	vorticity
Ω	dimensionless vorticity

REFERENCES

1. Hu Y, Bogy DB. Dynamic stability and spacing modulation of sub-25 nm fly height sliders. *Journal of Tribology* 1997; **119**:646–652.
2. Hu Y. Contact take-off characteristics of proximity recording air bearing sliders in magnetic hard disk drivers. *Journal of Tribology* 1999; **121**:948–954.
3. Berger EJ, Sadeghi F, Krousgrill CM. Finite element modeling of engagement of rough and grooved wet clutches. *Journal of Tribology* 1996; **118**:137–146.
4. Berger EJ, Sadeghi F, Krousgrill CM. Analytical and numerical modeling of engagement of rough, permeable, grooved wet clutches. *Journal of Tribology* 1997; **119**:143–148.
5. Kubo M, Ohtsubo Y, Kawashima N, Marumo H. Finite element solution for the rarefied gas lubrication problem. *Journal of Tribology* 1988; **110**:335–341.
6. Kotera H, Shima S. Shape optimization to perform prescribed air lubrication using genetic algorithm. *Tribology Transactions* 2000; **43**:837–841.
7. Theodossiou VM, Sousa ACM. An efficient algorithm for solving the incompressible fluid flow equations. *International Journal for Numerical Methods in Fluids* 1986; **6**:557–572.
8. Ghia U, Ghia KN, Shin CT. High-resolutions for incompressible flow using the Navier–Stokes equations and a multigrid method. *Journal of Computation Physics* 1982; **48**:387–411.
9. Freitas CJ, Street RL, Findikakis AN, Koseff JR. Numerical simulation of three-dimensional flow in a cavity. *International Journal for Numerical Methods in Fluids* 1985; **5**:561–575.
10. Migeon C, Texier A, Pineau G. Effects of lid-driven cavity shape on the flow establishment phase. *Journal of Fluids and Structures* 2000; **14**:469–488.
11. Migeon C, Pineau G, Texier A. Three-dimensionality development inside standard parallelepipeic lid-driven cavity at $Re = 1000$. *Journal of Fluids and Structures* 2003; **17**:717–738.
12. Chen CL, Cheng CH. Buoyancy-induced flow and convection heat transfer in an inclined arc-shape enclosure. *International Journal of Heat and Fluid Flow* 2002; **23**:823–830.
13. Chen CL, Cheng CH. Numerical prediction of buoyancy-induced periodic pattern and heat transfer in a lid-driven arc-shape cavity. *Numerical Heat Transfer* 2003; **44**(Part A):645–663.
14. Chen CL, Cheng CH. Experimental and numerical study of mixed convection and flow pattern in a lid-driven arc-shape cavity. *Heat Mass Transfer* 2004; **41**:58–66.
15. Taneda S. Visualization of separating Stokes flows. *Journal of the Physical Society of Japan* 1979; **46**:1935–1942.